NANOELECTRONICS

Ultraflexible nanoelectronic probes form reliable, glial scar–free neural integration

Lan Luan,[1]* Xiaoling Wei,[2]* Zhengtuo Zhao,[2]* Jennifer J. Siegel,[3] Ojas Potnis,[2] Catherine A Tuppen,[2] Shengqing Lin,[2] Shams Kazmi,[2] Robert A. Fowler,[2] Stewart Holloway,[2] Andrew K. Dunn,[2] Raymond A. Chitwood,[3] Chong Xie[2]†

Implanted brain electrodes construct the only means to electrically interface with individual neurons in vivo, but their recording efficacy and biocompatibility pose limitations on scientific and clinical applications. We showed that nanoelectronic thread (NET) electrodes with subcellular dimensions, ultraflexibility, and cellular surgical footprints form reliable, glial scar–free neural integration. We demonstrated that NET electrodes reliably detected and tracked individual units for months; their impedance, noise level, single-unit recording yield, and the signal amplitude remained stable during long-term implantation. In vivo two-photon imaging and postmortem histological analysis revealed seamless, subcellular integration of NET probes with the local cellular and vasculature networks, featuring fully recovered capillaries with an intact blood-brain barrier and complete absence of chronic neuronal degradation and glial scar.

INTRODUCTION

Chronically implanted electrodes (*1*–*4*) enable one of the most important neurotechniques by allowing for the acquisition of individual neuron electrical activities in the living brain (*5*–*7*). Although long-term electrical recording was sometimes observed (*2*, *8*), large variations in chronic recording capacity were often reported (*3*, *4*), largely due to the lack of stability at the interface between conventional electrodes and the brain tissue (*4*, *9*) in both the short and the long term. Conventional neural implants have volumes and surgical footprints considerably larger than those of cells and capillaries, which induce substantial damage and disruption to local cellular and vascular networks (*10*). Moreover, these probes are significantly more rigid than the host brain tissue, whose natural micromovements induce intense stress at the interface (*11*). In the short term, the resulting electrode displacement from their targeted neurons leads to sudden waveform changes in time scales as short as hours that prevent reliable tracking of individual neurons over days and longer (*12*, *13*). In the long term, the presence of implants causes recurring cellular and vascular damage, elicits sustained inflammation and tissue response (*14*), and eventually leads to neuronal degradation and glial scar formation near the implants (*10*, *15*, *16*). These chronic deteriorations are manifested in electrical recordings as degradations in recording fidelity, including increasing impedance, elevated noise levels, decreasing signal amplitudes, and diminishing unit recordings (*1*–*4*, *16*).

Extensive research efforts in the past decade have demonstrated that reducing the neural probe dimension (*17*) and rigidity (*16*, *18*, *19*) improves neural interface. Recent work has shown that macroporous electronics (*20*) and ultrasmall microelectrodes made of carbon fibers (*21*, *22*) greatly reduced tissue response. However, reliable brain probes that detect and track activities from the same neurons for extended periods with none of the aforementioned chronically detrimental effects require seamless biointegration but are yet to be demonstrated.

Taking previous efforts in improving the neural electrode interface into consideration, we identified the following key aspects for establishing a reliable and glial scar–free neural-probe interface: (i) the dimension of the probe is comparable to or smaller than that of average cells and capillaries, such that its perturbation to the host biological matrix is minimal (*10*, *17*); (ii) the probe has sufficient flexibility to ensure complete compliance to tissue micromovements and to reduce probe-tissue interfacial force to the range of cellular force (nanonewtons) (*20*, *23*); (iii) the surgical damage during implantation is less than ca. 100 μm across to allow for tissue recovery (*24*, *25*); and (iv) the probe is mechanically and electrically robust for long-term functionality under physiological conditions. To meet these stringent requirements, we developed ultraflexible nanoelectronic thread (NET) brain probes and an implantation strategy with cellular-sized surgical footprints. We verified the effectiveness of our approach in a rodent (mouse) model by chronic electrical recording and comprehensive characterizations of the probe-tissue interface.

RESULTS

We designed and fabricated two types of NET brain probes, NET-50 and NET-10, using a multilayer, substrate-less architecture and specialized photolithography (Materials and Methods). As shown in Fig. 1, NET-50 had a four-layer layout with a total thickness of 1 μm and an average width of 50 μm, hosting a linear array of eight electrodes. NET-10 featured a cross section of 10 μm × 1.5 μm, the smallest among all reported neural probes to the best of our knowledge, hosting four electrodes on two opposite surfaces in a seven-layer layout. To minimize volume and maximize flexibility, both types had electrodes and interconnects on different layers electrically connected by vias through the insulation layers. NET-50 probes were designed analogous to the commonly used silicon neural probe (for example, a single slab in NeuroNexus A8×8 design), whereas NET-10 probes were designed to offer similar recording characteristics to tetrodes (*1*, *3*), both with aggressively reduced dimensions (fig. S1). Compared with previously demonstrated neural probes (*18*, *21*, *26*), the NET probes drastically reduced the effective bending stiffness and tissue displacement per electrode for markedly improved biocompatibility (fig. S2). Specifically, the bending stiffness was reduced by orders of

[1]Department of Physics, the University of Texas at Austin, TX 78712–1192, USA. [2]Department of Biomedical Engineering, the University of Texas at Austin, TX 78712–1192, USA. [3]Center for Learning and Memory, Institute for Neuroscience, the University of Texas at Austin, TX 78712–1192, USA.
*These authors contributed equally to this work.
†Corresponding author. Email: chongxie@utexas.edu
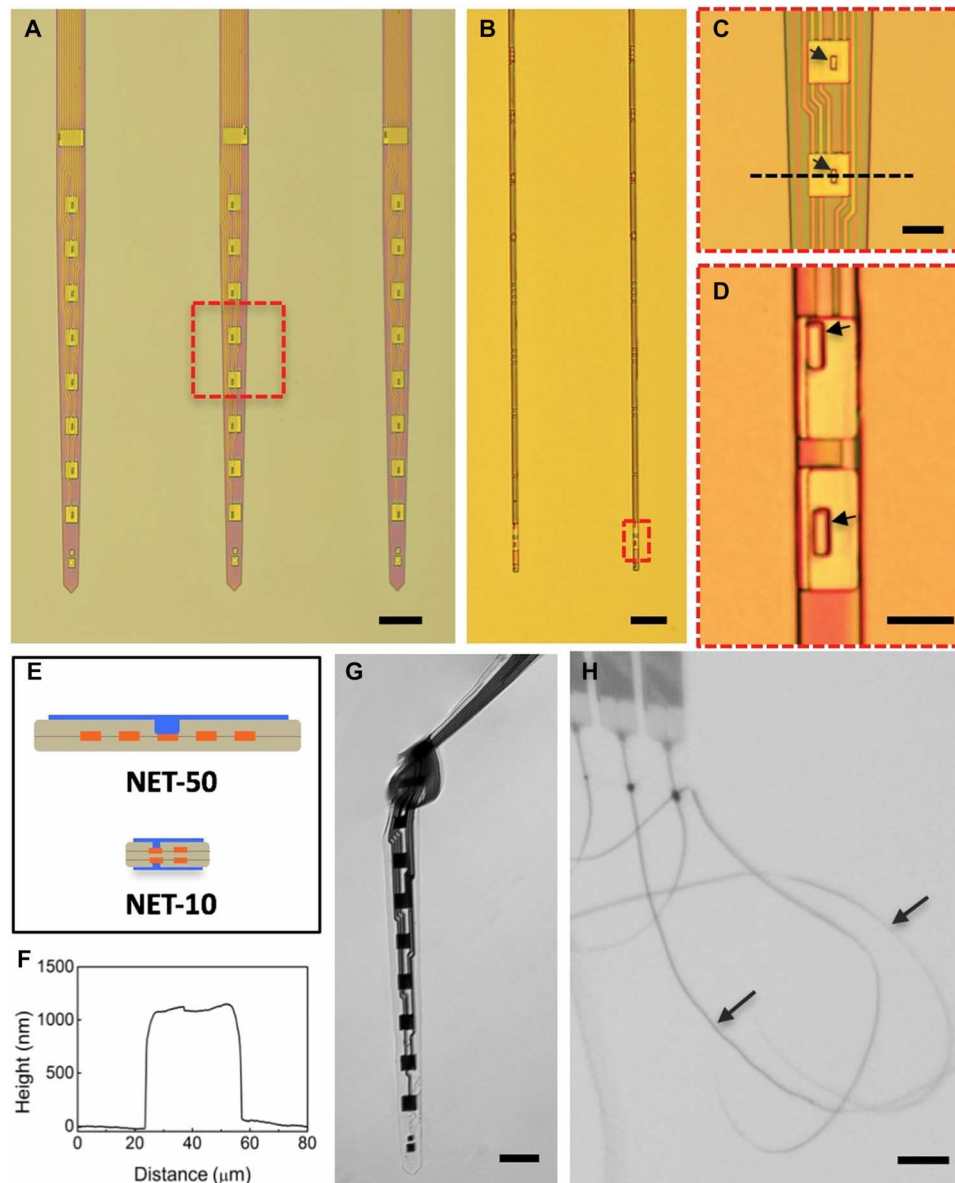
Fig. 1. Structures of NET neural probes. (**A** and **B**) As-fabricated NET-50 and NET-10 probes on substrates. (**C** and **D**) Zoom-in views of two electrodes as marked by the dashed boxes in (A) and (B), respectively. Arrows denote "vias." (**E**) Schematics of the probe cross section in (A, top) and (B, bottom), highlighting the multilayer layout. Color code: gray, insulation; orange, interconnects; and blue, electrodes. Not drawn to scale. (**F**) Height profile of the NET-50 probe along the dashed line in (C) measured by an atomic force microscope. (**G**) A NET-50 probe suspended in water. A knot is made with a curvature of less than 50 μm to illustrate its flexibility and robustness. (**H**) Multiple NET-10 probes suspended in water. Arrows denote the probes. Scale bars, 100 μm (A), 50 μm (B, G, and H), and 10 μm (C and D).

magnitude to 10^{-15} N·m², which brought down the probe-tissue interfacial force to the nanonewton range (fig. S3), on par with the single-cell traction forces (27).

The ultraflexibility of the NET probes mechanically precluded their self-supported penetration through brain tissue. Previous strategies for delivering flexible probes included temporarily altering the probe's rigidity (20) and, more commonly, temporarily attaching the probe to a rigid shuttle device (18, 19, 23, 28–31). However, most shuttle devices used in previous studies had dimensions larger than 100 μm, which were significantly larger than the dimensions of the NET probes and resulted in unrecoverable damage and persistent scarring (24, 25). We reduced the implantation footprints by about 10-fold to the cellular

dimensions by using a temporary engaging mechanism (Fig. 2A) and shuttle devices made of carbon fibers and tungsten microwires with diameters as small as 7 μm (Fig. 2B). The engaging mechanism was enabled by a micropost at the end of each shuttle device fabricated using focused ion beam (FIB) (fig. S4). During delivery, the micropost engaged into the microhole (Fig. 2, C to E) and pulled the NET probe to the desired depth (movie S1), after which the shuttle device disengaged and retracted (Materials and Methods). The overall insertion footprint was as small as ca. 10 μm across (Fig. 2, D and E), which led to only cellular-sized surgical damage, as evidenced by little bleeding (Fig. 2, F and G) and small insertion force (fig. S4). Taking advantage of the ultraflexibility and the ultrasmall dimensions, we accommodated
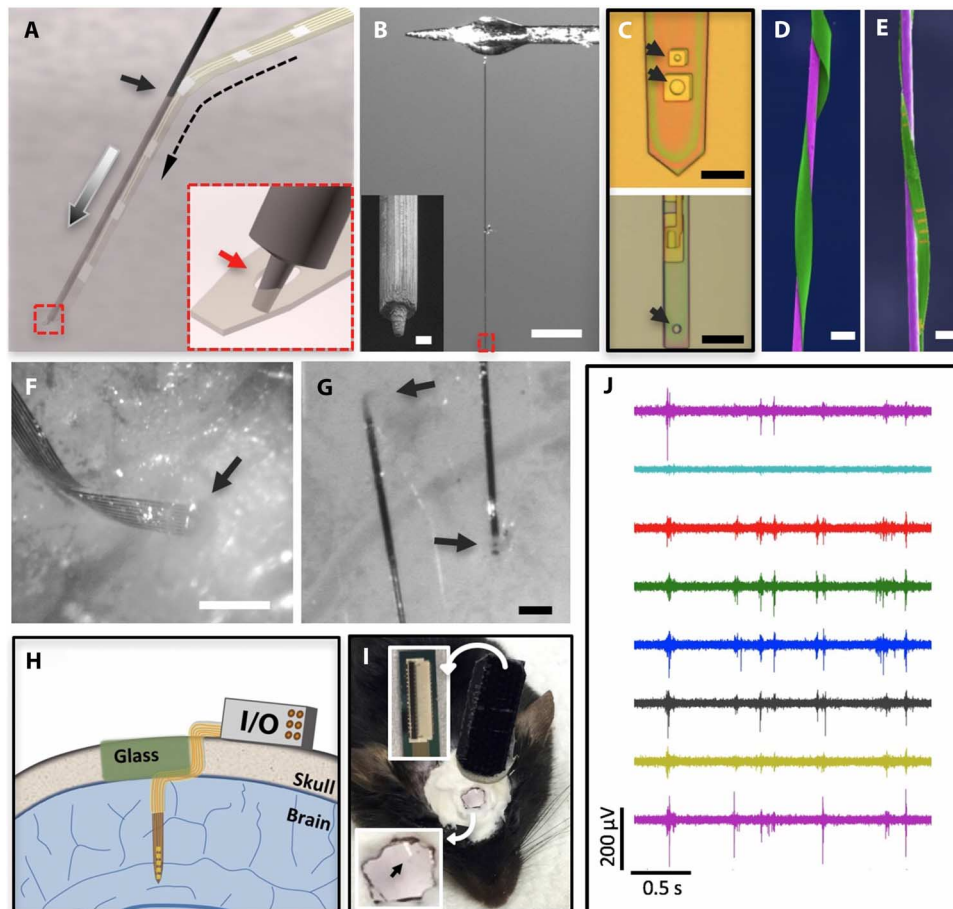
Fig. 2. Implantation procedure for the NET probes. (**A**) Schematic showing the temporary engaging mechanism. Arrows denote the entry site of the implantation (solid), the delivery path of the shuttle device (gray), and the path of the engaged NET probe (dashed). Inset: Zoom-in view of the dashed square highlighting that the micropost engages in the microhole on the NET probe at the end of the shuttle device. (**B**) Photograph of a typical carbon fiber shuttle device, with a diameter of 7 μm and a length of 3 mm, mounted at the end of a micromanipulator. Scale bar, 500 μm. Inset: Scanning electron microscopy (SEM) image of the micromilled post with a diameter of 2 μm and a height of 5 μm at the shuttle device tip. Scale bar, 2 μm. (**C**) Optical micrographs showing engaging holes in NET-50 (top) and NET-10 (bottom) probes with a slightly larger diameter than the post, as denoted by the arrows. (**D** and **E**) False-colored SEM images of NET-50 and NET-10 probes (green) attached on shuttle devices with a 20-μm tungsten microwire (D, purple) and a 10-μm carbon fiber (E, purple) showing their ultrasmall dimensions. Scale bars, 50 μm (D) and 20 μm (E). (**F** and **G**) Micrographs showing that both NET-50 and NET-10 probes were successfully delivered into the living mouse brain with minimal acute tissue damage. Arrows denote the delivery entry sites. Scale bars, 100 μm (F) and 50 μm (G). (**H**) Schematic of skull fixation that accommodates both connectors for the neural probes and a glass window allowing optical access. Not drawn to scale. (**I**) Photograph of a typical postsurgery mouse with implanted NET probes and a glass window mounted on top. Insets: top, image of a cable connector mounted on the skull; bottom, zoom-in view of the glass window in which the arrow denotes an implanted probe. (**J**) Typical unit activities recorded by eight electrodes on an implanted NET-50 probe. A high-pass filter (300 Hz) was applied.

chronic optical access with NET implants (Fig. 2, H and I), which allowed for monitoring of the tissue-probe interface by in vivo two-photon (2P) imaging. The electrical integrity was maintained throughout surgery and the implanted electrodes readily detected unit activities (Fig. 2J).

We next evaluated the long-term reliability of the NET probes. We implanted 16 probes into the somatosensory and visual cortices of seven mice, containing a total of 80 of the 96 connected electrodes (83.3% fabrication yield). We performed electrical recording on anesthetized animals twice a month for 4 months (Materials and Methods). We observed that recording performance improved during the initial 1.5 months and then remained stable for at least another 2.5 months (until the conclusion of our experiment period) in the following aspects: First, the average impedance and the noise level of all 80 electrodes decreased in the first 1.5 months and remained stable (Fig. 3A). Second, the num-

ber of electrodes that detected unit events and sortable single-unit action potentials (APs) increased in the first 1.5 months and then remained at the same level (Fig. 3B; examples of unit activities that include both nonsortable spikes and sortable single-unit APs are detailed in fig. S5). The yields of multi-unit (~75%) and sortable single-unit recording (~25%) were on par with conventional silicon probes for spontaneous measurement under anesthesia (32), but with unprecedented chronic stability. Third, we detected sortable AP waveforms from 19 electrodes with average amplitude and signal-to-noise ratio (SNR) being stable throughout the 4-month period (Fig. 3C).

We followed all 80 electrodes for 4 months and summarized their animal- and probe-specific performance over time in table S1 and fig. S5. Although there were variations in the number of functional electrodes and the unit detection yield among different animals, stability and consistency in unit detection over time were observed in all animals. As
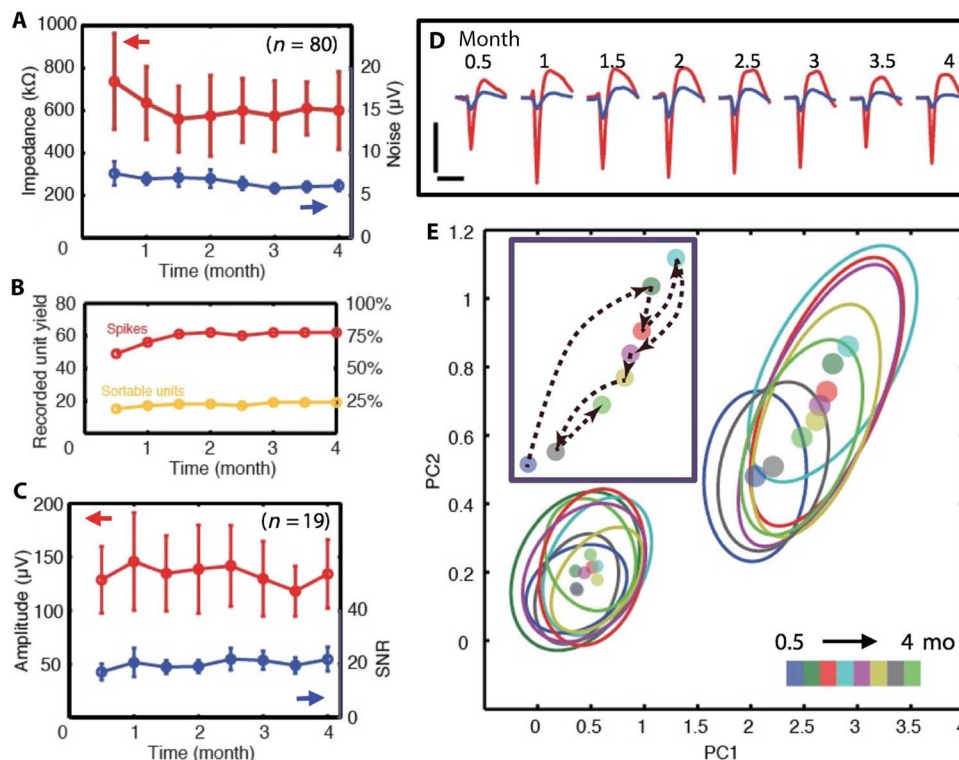
Fig. 3. Chronic recording and electrical characterization of implanted NET electrodes. (**A**) Impedance (red) and noise level (blue) of 80 implanted electrodes as a function of time. Error bars mark the SD. (**B**) The number (left) and percentage (right) of electrodes that recorded unit activities (red) and sortable single-unit APs (orange) as a function of time. (**C**) Average peak-valley amplitude (red) and SNR (blue) of single-unit APs recorded by $n = 19$ electrodes as a function of time. Error bars indicate the SD. (**D**) Twice-a-month measurements for 4 months from one electrode that recorded both nonsortable spikes (blue) and sortable AP waveforms (red). The waveforms are isolated and averaged from 3- to 9-min recording segments. Vertical bar, 200 μV; horizontal bar, 1 ms. (**E**) Principal component (PC) analysis of all the waveforms in (D). Dots: center of the PC. Ovals: 2σ contour of PC distribution. Colors code the time stamps. Inset: The evolution over time of the centers of the PC for the single-unit waveform.

an example, Fig. 3D shows the bimonthly measurements from the electrode that detected typical spike events and sortable AP waveforms with the highest SNR (>30) among all electrodes. The persistently high SNR of the sortable AP waveforms indicated that the firing neuron remained in close proximity to the electrode for the entire duration of the chronic recording (33). Combined principal component analysis for all measurements showed largely overlapping clusters with cluster centers' average position shifts between consecutive measurements equivalent to 0.88σ of the average cluster distribution (Fig. 3E), suggesting that the waveforms were generated by the same neuron. In addition, we repeatedly detected interneuron waveforms from one electrode (fig. S6), which were rare events (<10%) and served as a high-probability marker for tracking the same neuron (34). Furthermore, we observed persistent characteristics in AP waveforms, whereas minor trackable changes occurred for all except one electrode (18 of 19, 94.7%; fig. S7). Significantly, in contrast to previous neuron probes where decreasing amplitudes were typically observed over time, most of the NET electrodes recorded AP waveforms with nonmonotonic changes in peak-valley amplitude. The recording evidence strongly indicates that the NET probes form a nondegrading, slowly evolving interface with neurons.

To directly investigate the nature of the probe-tissue interface, we monitored capillaries, astrocytes, and neurons around the NET probes by in vivo 2P imaging at the implantation sites for up to 3.5 months after surgery (Materials and Methods). Figure S8 shows the evolution of the vasculature, showing that the surgical damage led to minor local leakage of the blood-brain barrier (BBB) upon implantation, which lasted for at

most 1 month and was fully repaired in association with vascular remodeling. As shown in Fig. 4 (A and B) and movie S2, both types of NET probes were embedded in capillaries with normal density, morphology, and an intact BBB by 2 months. We measured the blood flow rate by line scans (Fig. 4, C and D) (35) and obtained similar values next to (420 ± 180 μm/s) and away from (450 ± 210 μm/s) the probe (Materials and Methods), confirming that capillary perfusion immediately next to the probe was normal. This is in strong contrast to conventional microelectrodes where continuous BBB leakage was observed in chronic in vivo imaging at the interface (36).

We imaged the astrocytes by in vivo staining (Materials and Methods) 3.5 months after implantation around a NET-50 probe (Fig. 4E and movie S3). We note that the imaged segment was unintentionally folded during implantation with a sub–100-μm curvature, which set the upper limit of tissue-probe stress for NET probes. We observed that the astrocytes near the probe surrounded only capillaries with normal density and morphology (similar to astrocytes from the contralateral hemisphere of the same mouse shown in fig. S9). We also performed postmortem histology (Materials and Methods) 5 months after implantation and observed normal neuron density (fig. S10A) and resting microglia (Fig. 4F) near the probe. Remarkably, direct contact with the probe did not affect the viability of neurons, nor did it activate microglia (Fig. 4F) (24). These results show that the NET probes have unprecedented biocompatibility as they maintain normal vascular and cellular structures and elicit no observable chronic tissue reactions at the interface.
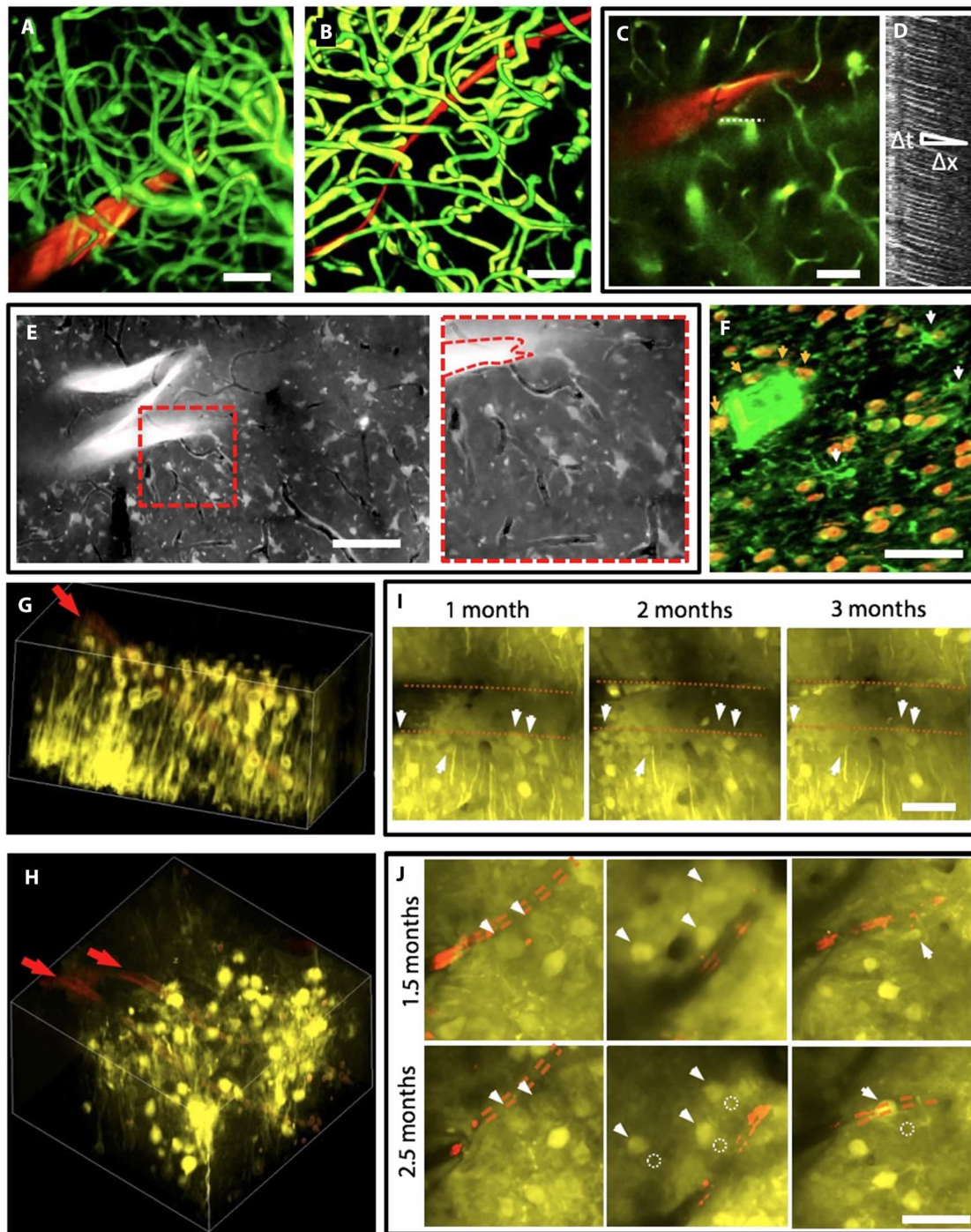
Fig. 4. Imaging and tracking of the cellular and vascular structures at the chronic probe-tissue interface. (**A** and **B**) Three-dimensional (3D) reconstruction of vasculatures by in vivo 2P microscopy around NET-50 (A) and NET-10 (B) probes (red) 2 months after implantation, highlighting fully recovered capillary networks (green). Image stack: 0 to 400 μm (A) and 100 to 320 μm (B) below the brain surface. See movie S2 for a full view of (B). (**C**) 2P image at 200 μm deep marking the position of a capillary (dashed line) for the line scans in (D). (**D**) Matrix of line scans showing movement of RBCs as dark stripes, the slope of which gives the blood flow speed. (**E**) Projection of in vivo 2P images at 210 to 250 μm below the brain surface at 3.5 months after implantation showing normal astrocytes and capillaries. The bright "z"-shaped object is a folded NET-50 probe. The capillaries are visible as dark lines. Right: Zoom-in view of the dashed area. See movie S3 for the full image stack 125 to 360 μm below the brain surface. (**F**) Projection of confocal micrographs of an immunochemically labeled cross-sectional slice (30 μm thick, 5 months after implantation). False-color code: orange, NeuN, labeling neuron nuclei; green, Iba-1 labeling microglia. White arrows denote microglia soma. Orange arrows denote neurons in contact with the NET probe. (**G** and **H**) 3D reconstruction of in vivo 2P images of neurons (yellow) in Thy1-YFP mice surrounding a NET-50 probe (G) and two NET-10 probes (H) 2 and 2.5 months after implantation, respectively. The probes are in red and denoted by arrows. Imaging depth: (G) 130 to 330 μm below the brain surface, (H) 110 to 260 μm below the brain surface. (**I** and **J**) Representative 2P images from the same regions in (G) and (H), respectively, showing that neurons are repeatedly identified at different times after implantation. Red dashed lines mark the edge of the probes. Arrows and dashed circles highlight the current and previous locations of neurons, respectively. See movies S4 and S5 for the full image stack. All scale bars, 50 μm.

To reveal the evolution of the neural interface, we repeatedly imaged neurons in the vicinity of both types of NET probes up to 3 months after implantation and compared their locations relative to a few representative neurons and capillaries as position markers (movies S4 and S5 and Fig. 4, G to J). We observed that all neurons initially imaged near the probe were identified in later imaging sessions, which further proved that the NET probes did not induce chronic neuronal loss. Furthermore, although most neurons were relatively stationary, some show slow migrations (up to ca. 10 µm) over the course of a few weeks (Fig. 4, I and J). Notably, we observed no preference in their migration trajectories for moving toward or away from the NET probes.

DISCUSSION

The ultraflexibility of the NET probe prohibits conveniently advancing to and recording from more than one brain region using schemes similar to microdrives that are widely applied in silicon probes and tetrodes. Instead, recording from deeper brain regions or from different brain tissue depths can be realized by implanting NET probes patterned with more electrodes spanning a larger depth, especially given the unprecedented tissue compatibility demonstrated here. Accommodating more electrodes on one probe does not necessarily increase the probe's dimension, as we can further increase the fabrication resolution by using electron beam lithography techniques (37).

We have thoroughly examined our full fabrication process and identified that the loss of yield is mainly due to fabrication defects. Our fabrication involves seven photolithography steps using a manual mask aligner and three metal deposition steps, which makes it difficult to completely avoid microparticles and scratches. Furthermore, our design has narrow metal lines (the interconnects, 2 to 3 µm wide) routed over 5 mm, which is vulnerable to microdefects. We expect that one can significantly improve the fabrication yield by using automated photolithography tools that can eliminate most of the defect sources.

The NET probes can be readily fabricated in linear arrays, similar to the conventional silicon probes. We estimate that we can deliver up to 12 NET probes within 40 min on the basis of the demonstrated average delivery time of 3 min per probe. The closest interprobe spacing we have achieved is about 200 µm, as shown in Fig. 2G. The accuracy in interprobe space is currently determined by the accuracy in the initial positioning of the NET probe (under a stereomicroscope) on the brain surface before delivery, which has an uncertainty of up to 30 µm.

The NET probes performed stably in mice for at least 4 months, as evidenced by the intact device structure (fig. S10) and the stable impedance and recording performance (Fig. 3), which are sufficient for most scientific studies and warrant further research on their performance in longer-term implantation (on the order of years). We attribute the stable performance of NETs to their unconventional dimensions and design, which can be explained by the following aspects: (i) The most prevalent failure modes in conventional devices are structural degradations, such as cracking, blistering, and delamination (38), none of which were observed in chronically implanted NETs (fig. S10, B and C). This can be attributed to the fact that the ultrathin thickness of NETs (1 µm) greatly reduces the strain on the device upon deformation, which prevents the formation of structural defects. (ii) Another major failure mode in conventional polymer implants is delamination due to insufficient bonding at interfaces (39). In NET probes, the SU-8 insulating layer adheres mainly with another SU-8 layer by thermal curing and cross-linking, which eliminated this failure mode. (iii) Most polymers absorb water under physiological conditions, which may lead to electrical leakage that results in signal attenuation. However, the possible water absorption–induced leakage did not affect our long-term recording performance, mostly because it did not induce structural damage of the NET as shown above, likely due to the improved adhesion between layers and reduced stress. Furthermore, NET probes were soaked for several days in phosphate-buffered saline (PBS) and other water solutions before implantation, which preconditioned the SU-8 film to a saturated water absorption of 3.3% (40), such that no signal attenuation was observed after implantation. Consistent with no structural deterioration, electrochemical impedance spectroscopy (EIS) showed a high impedance, moderately capacitive circuit over a large frequency range (fig. S11), and little cross-talk was observed from adjacent electrodes (fig. S12).

A very recent study reported stable long-term recording in mice using mesh electrodes on a similar device platform (31). The consistency between their study and ours strongly supports the validity of using ultraflexible devices, particularly polymer-based devices with an overall thickness of about 1 µm, for long-term neural activity mapping. Here, we further reduced both the device width and the surgical footprint to cellular dimensions, such that no persistent glial scar was observed near the implants in our study. In addition, we characterized the interface not only by postmortem histology, which gave a "snapshot" assessment, but also by repeated in vivo imaging of thick tissue stacks, which unambiguously revealed the evolution of vascular and cellular networks around the implanted NET probes.

Combining the results from chronic recording and in vivo imaging, we gain a comprehensive understanding of the neural interface formed by the NET probes. In vivo imaging and histology studies revealed a chronic tissue response free interface, which provides the biological foundation for nondegrading recording performance. Moreover, because the interface is dynamically evolving, which involves remodeling of vasculature and other changes in the microbiological environment, both the neurons and the NET probes are not completely stationary over a time frame of a few months. Correspondingly, we observed neuron migrations at a few micrometers per month, which led to slowly evolving waveforms in chronic recordings that could be reliably tracked by measurements twice a month.

We demonstrated that the NET probes form reliable, glial scar–free integration with the living brain by chronic recording, in vivo 2P imaging, and postmortem characterization of the tissue-probe interface. The unprecedented chronic reliability and stability are expected to fundamentally advance both basic and applied neuroscience, as well as lead to substantial improvement in the brain-machine interface which can be applied to neuroprosthetics (41). Furthermore, the subcellular dimension probes provide new opportunities for high-density electrical recording by overcoming current physical limitations (42).

MATERIALS AND METHODS
NET brain probe fabrication and preparation
The NET brain probes were fabricated using specialized fabrication methods similar to those previously reported (20, 43). The multilayer probes were fabricated using photolithography on a nickel metal release layer deposited on a silicon substrate (900 nm SiO$_2$, n-type 0.005 V·cm, University Wafer). An SU-8 photoresist (SU-8 2000.5, MicroChem Corp.), which offers excellent tensile strength, ease of fabrication, and demonstrated durability in ultrathin structures (fig. S10) (20, 23, 43), was used to construct the insulating layers. We used the minimum thickness of the dielectric layer necessary for preventing more than 1% signal

attenuation through the capacitive coupling between the interconnects and the conductive medium surrounding the probe, which was determined to be about 500 nm for our probe geometry and material. Platinum or gold was used for electrodes (size: 30 μm × 30 μm for NET-50 and 10 μm × 20 μm for NET-10) and interconnects, respectively, both with a thickness of 100 nm. The different sizes and materials used for the electrodes contributed to most of the variation in impedance, as shown in Fig. 3A. After fabrication, a 33-pin flexible flat connectors (FFC) (series 502598, Molex) was mounted on the matching contact pads on the Si substrate. The implantable section of the probe was then soaked in nickel etchant (TFB, Transene Co. Inc.) for 2 to 4 hours at 25°C to release the free-standing portion of the probe, while the contact region remained attached to the substrate. The substrate was cleaved to the desired length before implantation.

Shuttle device fabrication and assembly

A straight segment of a carbon fiber or tungsten wire was attached to a stainless steel microneedle (prod# 13561–10, Ted Pella Inc.) for convenient handling. It was then cut to the designed length (2 to 3 mm) using FIB. An anchor post was micromilled at the tip of the shuttle device using FIB to shape a well-defined micropost (3 μm in diameter and 5 μm in height, fig. S4).

Animals and surgery

Wild-type male mice (C57BJ/6, 8 weeks old, Taconic) and male transgenic strain [B6.Cg-Tg(Thy1-YFP)16Jrs/J, to which yellow fluorescent proteins were expressed in neurons; The Jackson Laboratory] were used in the experiments. Mice were housed at the Animal Resources Center at the University of Texas (UT) at Austin (at a 12-hour light/dark cycle at 22°C, with food and water ad libitum).

Mice were anesthetized using isoflurane (3% for induction and maintained at 1 to 2%) in medical-grade oxygen. The skull was exposed and prepared by scalping the crown and removing the fascia and then was scored with the tip of a scalpel blade. A 3-mm × 3-mm square craniotomy was performed with a surgical drill over the somatosensory cortex. Dura mater was carefully removed to facilitate the delivery. After NET probe implantation (described below), the remaining flexible segment of the NET probe, which connected the bonding pad on the substrate with the electrodes inside the brain, was routed to the edge of the cranial opening. The exposed brain was then protected by artificial cerebrospinal fluid (ACSF) and coverslip #1 (Fisher Scientific) fit into the cranial opening. The space between the coverslip and the remaining skull was filled with Kwik-Sil adhesive (World Precision Instruments). After the skull was cleaned and dried, a layer of low-viscosity cyanoacrylate was applied over the skull. An initial layer of C&B-Metabond (Parkell Inc.) was applied over the cyanoacrylate and the Kwik-Sil adhesive. A second layer of Metabond was used to cement the coverslip and the NET carrier chip to the skull. All procedures complied with the National Institutes of Health guidelines for the care and use of laboratory animals and were approved by the UT Institutional Animal Care and Use Committee.

Neural probe delivery

In typical procedures, a flexible neural probe was placed on the brain surface where dura mater was removed. The shuttle device was vertically mounted on a micromanipulator (MP-285, Sutter Instrument) and positioned atop the engaging hole at the end of the probe. As the shuttle device traveled downward, the anchor post entered the hole and pulled the neural probe into the brain tissue. Once the neural probe reached the desired depth, the shuttle device was retracted, and the neural probe was released and left embedded in the brain tissue. Because the volume of both the shuttle device and the neural probe was minimized to reduce tissue damage, the delivery process was delicate. A few experimental details are important to the success of the delivery. First, the anchor post of the shuttle device needs to be microfabricated precisely according to the well-defined cylindrical shape as designed, so that it can fit into the engaging hole on the probe, can have sufficient mechanical strength for the delivery, and can be retracted out of the brain without pulling the probe out with it. Second, the axial direction of the shuttle device needs to be aligned with the insertion direction to minimize buckling. Third, ACSF needs to be added to the brain surface as the shuttle device drags the probe into the brain to float the remaining flexible segment and to minimize friction between the probe and the brain surface. By controlling the engaging location and the insertion depth, we delivered NET probes to specific regions of interest. Multiple-probe delivery was achieved by repeating the same process sequentially.

2P imaging

2P imaging was performed using a laser scanning microscope (Prairie Technology) equipped with a 20× water immersion objective (numerical aperture, 1.0; Zeiss) and a Ti:sapphire excitation laser (Mai Tai DeepSee, Spectra-Physics) from acute to up to 3.5 months after implantation. The laser was tuned to 810 to 910 nm for 2P excitation (power, 3.0 to 50 mW; dwell time, 4.0 to 6.0 μs). Fluorescence emissions were detected simultaneously by two standard photomultiplier tubes with a 595/50-nm filter (Semrock) for "red" fluorescence emission and a 525/70-nm filter (Semrock) for "green" fluorescence emission. Mice were anesthetized using isoflurane (3% for induction and 1.5% during experiment) in medical-grade oxygen to maintain full immobility during imaging and placed in a frame that stabilized the head on the microscope stage. For 2P imaging on capillaries, anesthetized animals were given fluorescein isothiocyanate (FITC)–dextran (0.1 ml, 5% w/v, Sigma-Aldrich) retro-orbitally to label blood vessels before imaging. For 2P imaging on astrocytes, anesthetized animals were given sulforhodamine 101 (44) (0.1 ml, Sigma-Aldrich) and Optison (GE Healthcare, 0.1 ml) retro-orbitally. Immediately following the injection, focused ultrasound with a center frequency of 2.25 MHz in the tone burst mode (rate, 20 Hz; burst duration, 10 ms; duty cycle, 20%) was applied to the regions of interest for 45 s to temporarily break the BBB (45). Animals were imaged 2 hours after ultrasound treatment to ensure sufficient dye diffusion and staining. To facilitate the imaging of the probe-tissue interface beyond superficial cortical layers, we doped the probes with sulforhodamine 6G (Sigma-Aldrich) in the insulating layers and delivered them at about 45° with respect to the skull.

Line scan and blood flow speed

We inferred the blood flow speed from the motion of red blood cells (RBCs) shown as stripes in line-scan measurements, that is, repetitive scans of the laser along the central axis of a capillary. The animal was given FITC-dextran (0.1 ml, 5% w/v, Sigma-Aldrich) retro-orbitally before imaging. After obtaining a 2P image of capillaries at the desired depth, we identified a capillary of interest and electromechanically oriented the direction of the scan along it. We typically scanned a distance of 30 to 40 μm with 128 pixels per line, repeating 128 to 256 times at 1 to 2 ms per scan. We imaged nine capillaries in the vicinity of a NET-50 probe and six capillaries from the contralateral hemisphere

of the same mouse. The blood flow speed was 420 ± 180 μm/s near the probe, similar to 450 ± 210 μm/s away from the probe.

Histological sample preparation

Mice were given lethal intraperitoneal injections of 0.15 ml of ketamine mixed with xylazine [xylazine (10 mg/ml) in ketamine (90 mg/ml)] and then perfused intracardially with oxygenated, cold (~4°C) modified ACSF (2.5 mM KCl, 1.25 mM NaH_2PO_4, 25 mM $NaHCO_3$, 0.5 mM $CaCl_2$, 7 mM $MgCl_2$, 7 mM dextrose, 205.5 mM sucrose, 1.3 mM ascorbic acid, and 3.7 mM pyruvate) followed by 4% paraformaldehyde in 0.02 M PBS. Brains were cryoprotected in a 30% sucrose/4% paraformaldehyde solution overnight. Tissue was sectioned into 20- to 50-μm slices perpendicular to the probe using a Leica CM1950 cryostat (Leica Microsystems). The slices were washed (3×5 min) and incubated in hot sodium citrate solution (85°C to 95°C, 0.01 M in H_2O) for 30 min for antigen retrieval. Then, the slices were washed (3×5 min), incubated in blocking solution and permeabilized [0.5% Triton X-100 and 10% normal goat serum (Sigma-Aldrich) in PBS] for 3 hours at room temperature, washed (4×5 min), and incubated in fluorophore-conjugated antibodies for 24 hours at 4°C.

Reagents used for different cell types are as follows (Millipore): neurons: Alexa Fluor 488–conjugated anti-NeuN antibody, clone A60; microglia: Alexa Fluor 647–conjugated anti–glial fibrillary acidic protein antibody, clone GA5.

Neural recording

Voltage signals from the neural electrodes were amplified and digitized using a 32-channel RHD2132 evaluation system (Intan Technologies) with a bare Ag wire inserted into the contralateral hemisphere of the brain as the grounding reference. The animal was anesthetized with 1.5% isoflurane in medical-grade O_2 during the measurement. The sampling rate was 20 kHz, and a 300-Hz high-pass filter and a 60-Hz notch filter were applied for single-unit recording. The impedance of the electrodes was measured using the same equipment at 1000 Hz. Variation in impedance was mostly attributed to the different sizes and materials of the electrodes (materials: Pt/Au; sizes: 30 μm × 30 μm for NET-50 and 10 μm × 20 μm for NET-10). Spike detection and spike sorting were performed using Offline Sorter (Plexon).

SUPPLEMENTARY MATERIALS

Supplementary material for this article is available at http://advances.sciencemag.org/cgi/content/full/3/2/e1601966/DC1

fig. S1. Sketch showing the subcellular cross-section areas of the NET probes in comparison with other representative neural probes.
fig. S2. Drastically reduced bending stiffness and tissue displacement per electrode of the NET probes compared with other representative neural probes.
fig. S3. In vitro measurement of the bending force from suspended NET probes.
fig. S4. Shuttle device fabrication and in vivo insertion force measurement.
fig. S5. Typical unit recording examples and their detection consistency over 4 months.
fig. S6. Interneuron recording and tracking compared between a NET-50 electrode and a tetrode.
fig. S7. Twice-a-month measurements for 4 months from all electrodes that recorded sortable single-unit APs.
fig. S8. 3D reconstruction of 2P images of the capillary networks (green) surrounding two NET-50 probes (red) at acute, 1 week, 1 month, and 2 months after implantation.
fig. S9. Z projections of in vivo 2P images of astrocytes from the contralateral hemisphere of the same mouse as in Fig. 4E.
fig. S10. Bright-field and fluorescent images of postmortem tissue slices at the probe-tissue interface 5 months after implantation.
fig. S11. In vitro EIS of a NET electrode that was soaked in saline at 37°C for 35 days.
fig. S12. Real-time recording trace (300 Hz high-pass filter applied) from two adjacent channels showing distinct features and little cross-talk.

table S1. Animal- and probe-specific recording performance over time.
movie S1. A typical implantation procedure of the NET probe.
movie S2. The NET-vasculature integration 2 months after implantation.
movie S3. In vivo 2P images of inactive astrocytes and intact capillary network around a folded segment of a NET-50 probe 3 months after implantation.
movie S4. In vivo 2P images of neurons and two NET-10 probes 1.5 and 2.5 months after implantation.
movie S5. 3D reconstruction of in vivo 2P images of neurons and two NET-10 probes 1.5 months after implantation (the same images as in movie S4, left).
References (46, 47)

REFERENCES AND NOTES

1. C. M. Gray, P. E. Maldonado, M. Wilson, B. McNaughton, Tetrodes markedly improve the reliability and yield of multiple single-unit isolation from multi-unit recordings in cat striate cortex. *J. Neurosci. Methods* **63**, 43–54 (1995).
2. M. A. Nicolelis, D. Dimitrov, J. M. Carmena, R. Crist, G. Lehew, J. D. Kralik, S. P. Wise, Chronic, multisite, multielectrode recordings in macaque monkeys. *Proc. Natl. Acad. Sci. U.S.A.* **100**, 11041–11046 (2003).
3. D. R. Kipke, R. J. Vetter, J. C. Williams, J. F. Hetke, Silicon-substrate intracortical microelectrode arrays for long-term recording of neuronal spike activity in cerebral cortex. *IEEE Trans. Neural Syst. Rehabil. Eng.* **11**, 151–155 (2003).
4. P. J. Rousche, R. A. Normann, Chronic recording capability of the utah intracortical electrode array in cat sensory cortex. *J. Neurosci. Methods* **82**, 1–15 (1998).
5. A. P. Alivisatos, M. Chun, G. M. Church, R. J. Greenspan, M. L. Roukes, R. Yuste, The brain activity map project and the challenge of functional connectomics. *Neuron* **74**, 970–974 (2012).
6. M. E. Spira, A. Hai, Multi-electrode array technologies for neuroscience and cardiology. *Nat. Nanotechnol.* **8**, 83–94 (2013).
7. H. Shen, Neurotechnology: BRAIN storm. *Nature* **503**, 26–28 (2013).
8. M. Okun, A. Lak, M. Carandini, K. D. Harris, Long term recordings with immobile silicon probes in the mouse cortex. *PLOS ONE* **11**, e0151180 (2016).
9. V. S. Polikov, P. A. Tresco, W. M. Reichert, Response of brain tissue to chronically implanted neural electrodes. *J. Neurosci. Methods* **148**, 1–18 (2005).
10. J. P. Seymour, D. R. Kipke, Neural probe design for reduced tissue encapsulation in CNS. *Biomaterials* **28**, 3594–3607 (2007).
11. A. Gilletti, J. Muthuswamy, Brain micromotion around implants in the rodent somatosensory cortex. *J. Neural Eng.* **3**, 189–195 (2006).
12. G. W. Fraser, A. B. Schwartz, Recording from the same neurons chronically in motor cortex. *J. Neurophysiol.* **107**, 1970–1978 (2012).
13. J. A. Perge, M. L. Homer, W. Q. Malik, S. Cash, E. Eskandar, G. Friehs, J. P. Donoghue, L. R. Hochberg, Intra-day signal instabilities affect decoding performance in an intracortical neural interface system. *J. Neural Eng.* **10**, 036004 (2013).
14. J. C. Williams, R. L. Rennaker, D. R. Kipke, Long-term neural recording characteristics of wire microelectrode arrays implanted in cerebral cortex. *Brain Res. Brain Res. Protoc.* **4**, 303–313 (1999).
15. Y. Zhong, R. V. Bellamkonda, Biomaterials for the central nervous system. *J. R. Soc. Interface* **5**, 957–975 (2008).
16. J.-W. Jeong, G. Shin, S. I. Park II, K. J. Yu, L. Xu, J. A. Rogers, Soft materials in neuroengineering for hard problems in neuroscience. *Neuron* **86**, 175–186 (2015).
17. J. P. Seymour, D. R. Kipke, Fabrication of polymer neural probes with sub-cellular features for reduced tissue encapsulation. *Conf. Proc. IEEE Eng. Med. Biol. Soc.* **1**, 4606–4609 (2005).
18. T.-i. Kim, J. G. McCall, Y. H. Jung, X. Huang, E. R. Siuda, Y. Li, J. Song, Y. M. Song, H. A. Pao, R.-H. Kim, C. Lu, S. D. Lee, I.-S. Song, G. Shin, R. Al-Hasani, S. Kim, M. P. Tan, Y. Huang, F. G. Omenetto, J. A. Rogers, M. R. Bruchas, Injectable, cellular-scale optoelectronics with applications for wireless optogenetics. *Science* **340**, 211–216 (2013).
19. H. S. Sohal, A. Jackson, R. Jackson, G. J. Clowry, K. Vassilevski, A. O'Neill, S. N. Baker, The sinusoidal probe: A new approach to improve electrode longevity. *Front. Neuroeng.* **7**, 10 (2014).
20. C. Xie, J. Liu, T.-M. Fu, X. Dai, W. Zhou, C. M. Lieber, Three-dimensional macroporous nanoelectronic networks as minimally invasive brain probes. *Nat. Mater.* **14**, 1286–1292 (2015).
21. T. D. Kozai, N. B. Langhals, P. R. Patel, X. Deng, H. Zhang, K. L. Smith, J. Lahann, N. A. Kotov, D. R. Kipke, Ultrasmall implantable composite microelectrodes with bioactive surfaces for chronic neural interfaces. *Nat. Mater.* **11**, 1065–1073 (2012).
22. G. Guitchounts, J. E. Markowitz, W. A. Liberti, T. J. Gardner, A carbon-fiber electrode array for long-term neural recording. *J. Neural Eng.* **10**, 046016 (2013).
23. J. Liu, T.-M. Fu, Z. Cheng, G. Hong, T. Zhou, L. Jin, M. Duvvuri, Z. Jiang, P. Kruskal, C. Xie, Z. Suo, Y. Fang, C. M. Lieber, Syringe-injectable electronics. *Nat. Nanotechnol.* **10**, 629–636 (2015).

24. K. A. Potter, A. C. Buck, W. K. Self, J. R. Capadona, Stab injury and device implantation within the brain results in inversely multiphasic neuroinflammatory and neurodegenerative responses. *J. Neural Eng.* **9**, 046020 (2012).

25. T. D. Y. Kozai, Z. Gugel, X. Li, P. J. Gilgunn, R. Khilwani, O. B. Ozdoganlar, G. K. Fedder, D. J. Weber, X. T. Cui, Chronic tissue response to carboxymethyl cellulose based dissolvable insertion needle for ultra-small neural probes. *Biomaterials* **35**, 9255–9268 (2014).

26. H. Lee, R. V. Bellamkonda, W. Sun, M. E. Levenston, Biomechanical analysis of silicon microelectrode-induced strain in the brain. *J. Neural Eng.* **2**, 81–89 (2005).

27. O. du Roure, A. Saez, A. Buguin, R. H. Austin, P. Chavrier, P. Silberzan, B. Ladoux, Force mapping in epithelial cell migration. *Proc. Natl. Acad. Sci. U.S.A.* **102**, 2390–2395 (2005).

28. S. Felix, K. Shah, D. George, V. Tolosa, A. Tooker, H. Sheth, T. Delima, S. Pannu, Removable silicon insertion stiffeners for neural probes using polyethylene glycol as a biodissolvable adhesive. *Conf. Proc. IEEE Eng. Med. Biol. Soc.* **2012**, 871–874 (2012).

29. Z. L. Xiang, S.-C. Yen, N. Xue, T. Sun, W. M. Tsang, S. S. Zhang, L.-D. Liao, N. V. Thakor, C. Lee, Ultra-thin flexible polyimide neural probe embedded in a dissolvable maltose-coated microneedle. *J. Micromech. Microeng.* **24**, 065015 (2014).

30. T. D. Kozai, D. R. Kipke, Insertion shuttle with carboxyl terminated self-assembled monolayer coatings for implanting flexible polymer neural probes in the brain. *J. Neurosci. Methods* **184**, 199–205 (2009).

31. T.-M. Fu, G. Hong, T. Zhou, T. G. Schuhmann, R. D. Viveros, C. M. Lieber, Stable long-term chronic brain mapping at the single-neuron level. *Nat. Methods* **13**, 875–882 (2016).

32. T. D. Kozai, Z. Du, Z. V. Gugel, M. A. Smith, S. M. Chase, L. M. Bodily, E. M. Caparosa, R. M. Friedlander, X. T. Cui, Comprehensive chronic laminar single-unit, multi-unit, and local field potential recording performance with planar single shank electrode arrays. *J. Neurosci. Methods* **242**, 15–40 (2015).

33. P. Stratton, A. Cheung, J. Wiles, E. Kiyatkin, P. Sah, F. Windels, Action potential waveform variability limits multi-unit separation in freely behaving rats. *PLOS ONE* **7**, e38482 (2012).

34. P. L. Tierney, E. Degenetais, A.-M. Thierry, J. Glowinski, Y. Gioanni, Influence of the hippocampus on interneurons of the rat prefrontal cortex. *Eur. J. Neurosci.* **20**, 514–524 (2004).

35. D. Kleinfeld, P. P. Mitra, F. Helmchen, W. Denk, Fluctuations and stimulus-induced changes in blood flow observed in individual capillaries in layers 2 through 4 of rat neocortex. *Proc. Natl. Acad. Sci. U.S.A.* **95**, 15741–15746 (1998).

36. T. D. Y. Kozai, J. R. Eles, A. L. Vazquez, X. T. Cui, Two-photon imaging of chronically implanted neural electrodes: Sealing methods and new insights. *J. Neurosci. Methods* **258**, 46–55 (2016).

37. J. Scholvin, J. P. Kinney, J. G. Bernstein, C. Moore-Kochlacs, N. Kopell, C. G. Fonstad, E. S. Boyden, Close-packed silicon microelectrodes for scalable spatially oversampled neural recording. *IEEE Trans. Biomed. Eng.* **63**, 120–130 (2016).

38. G. Schmitt, F. Faßbender, H. Lüth, M. J. Schöning, J.-W. Schultze, G. Buß, Passivation and corrosion of microelectrode arrays. *Mater. Corros.* **51**, 20–25 (2000).

39. P. J. Gilgunn, X. C. Ong, S. N. Flesher, A. B. Schwartz, R. A. Gaunt, Structural analysis of explanted microelectrode arrays, International IEEE/EMBS Conference in Neural Engineering (NER 2013), San Diego, CA, 6 to 8 November 2013.

40. L.-h. Tam, D. Lau, Moisture effect on the mechanical and interfacial properties of epoxy-bonded material system: An atomistic and experimental investigation. *Polymer* **57**, 132–142 (2015).

41. L. R. Hochberg, G. M. Friehs, J. A. Mukand, M. Saleh, A. H. Caplan, A. Branner, D. Chen, R. D. Penn, J. P. Donoghue, Neuronal ensemble control of prosthetic devices by a human with tetraplegia. *Nature* **442**, 164–171 (2006).

42. A. H. Marblestone, B. M. Zamft, Y. G. Maguire, M. G. Shapiro, T. R. Cybulski, J. I. Glaser, D. Amodei, P. B. Stranges, R. Kalhor, D. A. Dalrymple, D. Seo, E. Alon, M. M. Maharbiz, J. M. Carmena, J. M. Rabaey, E. S. Boyden, G. M. Church, K. P. Kording, Physical principles for scalable neural recording. *Front. Comput. Neurosci.* **7**, 137 (2013).

43. B. Tian, J. Liu, T. Dvir, L. Jin, J. H. Tsui, Q. Qing, Z. Suo, R. Langer, D. S. Kohane, C. M. Lieber, Macroporous nanowire nanoelectronic scaffolds for synthetic tissues. *Nat. Mater.* **11**, 986–994 (2012)

44. A. Nimmerjahn, F. Kirchhoff, J. N. D. Kerr, F. Helmchen, Sulforhodamine 101 as a specific marker of astroglia in the neocortex in vivo. *Nat. Methods* **1**, 31–37 (2004).

45. E. E. Konofagou, Optimization of the ultrasound-induced blood–brain barrier opening. *Theranostics* **2**, 1223–1237 (2012).

46. M. A. L. Nicolelis, A. A. Ghazanfar, B. M. Faggin, S. Votaw, L. M. O. Oliveira, Reconstructing the engram: Simultaneous, multisite, many single neuron recordings. *Neuron* **18**, 529–537 (1997).

47. P. J. Rousche, D. P. Pivin , J. C. Williams, R. J. Vetter, D. R. Kipke, Flexible polyimide-based intracortical electrode arrays with bioactive capability. *IEEE Trans. Biomed. Eng.* **48**, 361–371 (2001).

Luan *et al. Sci. Adv.* 2017;**3**:e1601966   15 February 2017

9 of 9

Science Advances

Ultraflexible nanoelectronic probes form reliable, glial scar–free neural integration

Lan Luan, Xiaoling Wei, Zhengtuo Zhao, Jennifer J. Siegel, Ojas Potnis, Catherine A Tuppen, Shengqing Lin, Shams Kazmi, Robert A. Fowler, Stewart Holloway, Andrew K. Dunn, Raymond A. Chitwood and Chong Xie (February 15, 2017)

The following resources related to this article are available online at http://advances.sciencemag.org. (This information is current as of February 23, 2017):

Updated information and services, including high-resolution figures, can be found in the online version of this article at:
http://advances.sciencemag.org/content/3/2/e1601966.full

Supporting Online Material can be found at:
http://advances.sciencemag.org/content/suppl/2017/02/13/3.2.e1601966.DC1

This article **cites 46 articles,** 6 of which you can access for free at:
http://advances.sciencemag.org/content/3/2/e1601966#BIBL